Wind Tunnel and Hover Performance Test Results for Multicopter UAS Vehicles

Carl Russell
Aeromechanics Office
NASA Ames Research Center
Moffett Field, CA

Jaewoo Jung
Aviation Systems Division
NASA Ames Research Center
Moffett Field, CA

Gina Willink
Aeromechanics Office
NASA Ames Research Center
Moffett Field, CA

Brett Glasner
Universities Space Research Association
Moffett Field, CA

ABSTRACT

There is currently a lack of published data for the performance of multicopter unmanned aircraft system (UAS) vehicles, such as quadcopters and octocopters, often referred to collectively as drones. With the rapidly increasing popularity of multicopter UAS, there is interest in better characterizing the performance of this type of aircraft. By studying the performance of currently available vehicles, it will be possible to develop models for vehicles at this scale that can accurately predict performance and model trajectories. This paper describes a wind tunnel test that was recently performed in the U.S. Army's 7- by 10-ft Wind Tunnel at NASA Ames Research Center. During this wind tunnel entry, five multicopter UAS vehicles were tested to determine forces and moments as well as electrical power as a function of wind speed, rotor speed, and vehicle attitude. The test is described here in detail, and a selection of the key results from the test is presented.

NOMENCLATURE

BDAS	Basic Data Acquisition System
DELIVER	Design Environment for Novel Vertical Lift Vehicles
ESC	Electronic Speed Controller
FFT	Fast Fourier Transform
NDARC	NASA Design and Analysis of Rotorcraft
RVLT	Revolutionary Vertical Lift Technology
UAS	Unmanned Aircraft System
UTM	UAS Traffic Management
A	Rotor disk area, ft^2
C_T	Thrust coefficient, $T/\rho A(\Omega R)^2$
F_x, F_y, F_z	x-, y-, and z-force, lb
M_x, M_y, M_z	x-, y-, and z-moment, ft-lb
q	Dynamic pressure, lb/ft^2
R	Rotor radius, ft
T	Thrust, lb
α	Pitch angle, deg
ρ	Air density, slugs/ft^3
Ω	Rotor rotation speed, rad/s

INTRODUCTION

Multicopter unmanned aircraft have seen a rapid rise in production and utilization in the past few years. As the use of these vehicles continues to increase, research questions have emerged concerning their design, handling qualities, and control. In particular, three NASA projects/sub-projects—UAS Traffic Management (UTM), Design Environment for Novel Vertical Lift Vehicles (DELIVER), and Revolutionary Vertical Lift Technology (RVLT)—have an interest in determining the aerodynamic performance characteristics of multicopters.

DELIVER and RVLT are focused on advancing the state of the art in design and analysis tools for vertical lift vehicles [Ref. 1]. DELIVER is particularly focused on small (less than 2-passenger) alternative propulsion concepts. Both DELIVER and RVLT use a rotorcraft design software tool called NDARC (NASA Design and Analysis of Rotorcraft), which has been extensively validated for large (above 2-passenger) rotorcraft [Ref. 2]. Recently completed modifications to NDARC extended the propulsion models to include electric propulsion systems [Ref. 3]. The NDARC models should, in theory, be extensible to small multicopters, but have not yet been calibrated to existing aircraft. A research effort is currently underway to obtain data on small (up to approximately 10 lb) multicopters to aid in this calibration. The necessary data include rotor performance, airframe aerodynamics, battery and motor performance, and detailed component weights. The data gathered as part of this test will provide calibration data for rotor performance and airframe aerodynamics.

The UTM Project is developing a prototype system consisting of technologies that will enable safe, efficient operations in low-altitude, where a significant increase in unmanned aircraft flights is anticipated [Ref. 4]. Currently, the system shown in Fig. 1 is being considered as a prototype. One of the key requirements in implementing the system in Fig. 1 is an understanding of the capabilities of unmanned aircraft under a range of environmental conditions. In particular, there is a need to determine whether a given aircraft will be able to maintain control and/or station-keeping within a pre-defined area of airspace under forecasted weather conditions. Information that is

Presented at the AHS 72nd Annual Forum, West Palm Beach, FL, May 16-19, 2016.

critical to this type of understanding is the interaction between rotor RPM, vehicle air speed, and attitude on the forces and moments on the vehicle. The data collected from the test described here will be used to help populate the vehicle performance database shown in the top left of Fig. 1.

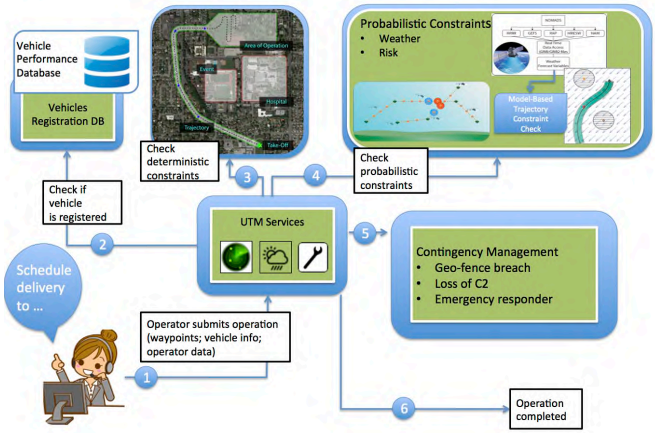

Figure 1. UTM system schematic.

The vast majority of published research on multicopters focuses on dynamics and control of the vehicles, with little on experimental performance data. In recent years, there have been some tests on the small propellers used for multicopters. In particular, Brandt and Selig [Refs. 5 and 6] published a database of propeller performance data including thrust and shaft power in axial flow in a wind tunnel as well as at static conditions. There have also been limited results published for small quadcopter propellers in edgewise flight, such as Ref. 7. Flight test data has also been used to estimate quadcopter performance and enhance simulation models [Ref. 8].

There is significant overlap between the data needs of the UTM, DELIVER, and RVLT research efforts, so a jointly planned wind tunnel test was executed to determine the aerodynamic performance characteristics of five different multicopter aircraft. The primary goal of the test was to generate a high-quality set of data for multicopter performance that can be used for model development and validation. The test took place in the U.S. Army 7- by 10-ft wind tunnel at NASA Ames Research Center. Measurements included forces and moments on the multicopter rotors and airframes as well as electrical power as a function of speed, attitude, and rotor RPM. Complementary testing was performed to measure hover performance of multicopter rotors and complete vehicles. This paper summarizes the wind tunnel and hover performance tests and presents a subset of the data collected.

TEST OVERVIEW

Five aircraft were tested as part of this wind tunnel entry: 3D Robotics (3DR) SOLO, DJI Phantom 3 Advanced, 3D Robotics Iris+, Drone America x8, and Straight Up Imaging (SUI) Endurance [Refs. 9 - 13]. All five aircraft are commercially available multicopters whose primary mission is photographic surveillance. Table 1 summarizes the pertinent details of the five aircraft, and Figs. 2-6 show pictures of the vehicles installed in the wind tunnel. In addition to the full vehicles, three of the isolated rotors were tested in the wind tunnel, and this configuration is shown in Fig. 7 for the SUI Endurance.

All of the vehicles were modified from their typical consumer configuration to facilitate testing in the wind tunnel, with internal electronic components being the most notable change. The brushless motors employed by all of the multicopters tested here require a three-phase switched DC power signal provided by an electronic speed controller (ESC). On production versions of the vehicles, the ESCs are typically embedded in custom circuit boards. Directly controlling the ESCs would therefore require access to the programming interface for the custom circuitry for each vehicle, which was an unnecessary complication for the test. Thus, the custom circuitry was removed and was replaced by off-the-shelf ESCs—one for each motor—for the wind tunnel test.

The other primary modification was the removal of the camera gimbals in order to use the gimbal mounting holes to install the vehicles in the wind tunnel test section. Both the interface with the ESCs and the physical interface with the test vehicles are discussed further in the following section.

Table 1. Multicopter Test Vehicles.

Make/Model	Configuration	Rotor-to-Rotor Length, in	Rotor-to-Rotor Width, in	Rotor Diameter, in	Nominal Flight Weight, lb★
3DR SOLO	Quadcopter	11.5	11.5	10.0	3.3
DJI Phantom 3	Quadcopter	9.8	9.9	9.4	2.8
3DR Iris+	Quadcopter	10.4	16.1	9.6	2.8
Drone America x8	Octocopter	31.4	31.4	11.0	12.8
Straight Up Imaging Endurance	Quadcopter	20.1	20.1	15.0	6.0

★Without additional payload

Figure 2. 3D Robotics SOLO.

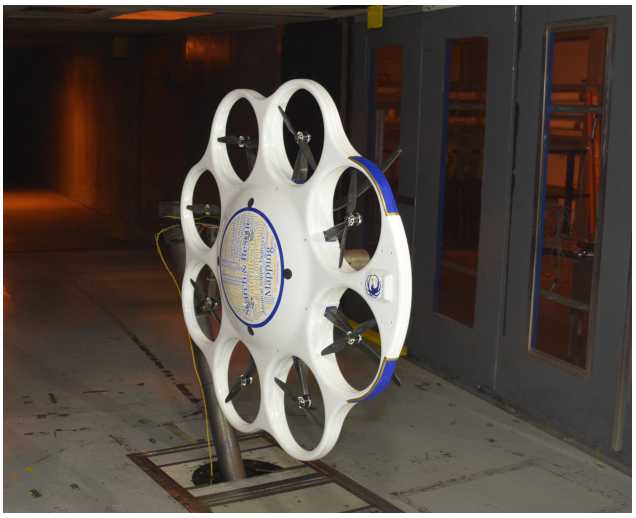

Figure 5. Drone America DAx8.

Figure 3. DJI Phantom 3 Advanced.

Figure 6. SUI Endurance.

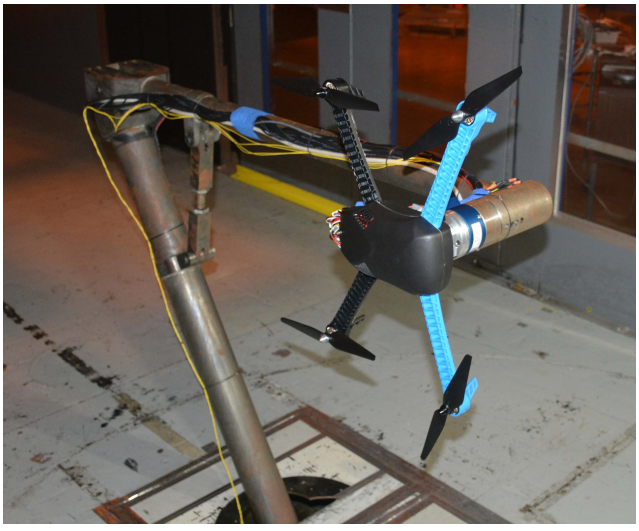

Figure 4. 3D Robotics Iris+.

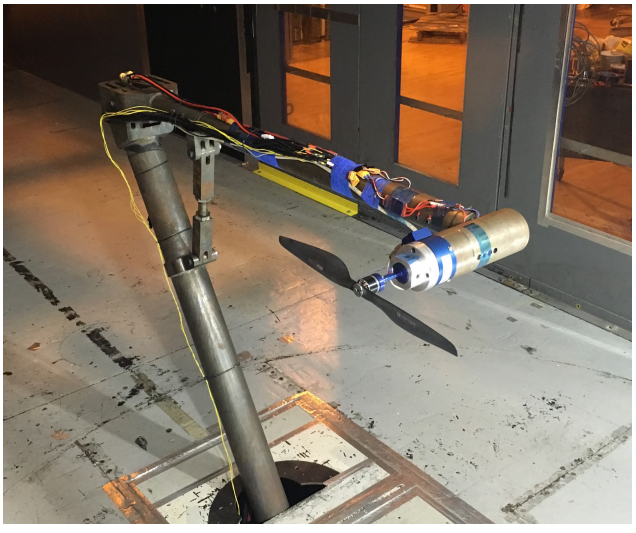

Figure 7. Isolated rotor – SUI Endurance.

TEST DETAILS

The objective of the test was to measure forces, moments, and motor power as a function of wind speed, attitude, and rotor RPM for each test vehicle. Each of the five multicopter aircraft was run through a range of test conditions, including the full airframe, bare airframe, and propeller only.

The following sections detail the data acquisition and model control systems that were used to meet the test objectives. Next, the model mounting hardware is described, followed by an overview of the testing procedures. Finally, the steps taken to reduce and correct the data are described.

Test Control and Measurement Systems

An overview of the test systems used for data acquisition, model control, and power delivery is shown in the schematic in Fig. 8, and is described below. These aircraft normally fly either autonomously or under radio control with batteries providing power. To eliminate battery safety concerns and eliminate testing downtime that would be required for battery charging, power was provided by a 3,000-watt Sorensen DC power supply. The power supply is capable of supplying up to 20 V DC power at up to 150 A, which is sufficient to power each of the test vehicles up to their respective maximum power.

Two different data acquisition systems were used to collect data for this test. The primary data system was the Basic Data Acquisition System (BDAS), which is a LabVIEW-based system that can be configured to record tunnel conditions in addition to user data signals [Ref. 14]. For this test, the user data included the model angle of attack, the model forces and moments, and the voltage and current to each ESC. These signals were passed through a Pacific Instruments signal conditioning system to the BDAS system, which collected data at a rate of 1,024 samples per second and then computed the average over a 30 second data record.

The secondary data system contained both the software for commanding the ESC and a second LabVIEW program for recording rotor RPM. This system recorded the rotor RPM and also provided a real-time display of RPM for each motor. Rotor speed control inputs were made by a human in the loop (usually the test engineer), to match the target RPM. Radio control of the test vehicles was undesirable due to concerns about radio interference. Control was therefore accomplished via a servo controller with a wired connection to the test article. The Pololu Mini Maestro servo controller has outputs for up to 12 servos, which can be controlled independently. The pulse-width modulated (PWM) signal used by RC aircraft servos is the same as that used by the ESCs, so this servo controller provides a convenient means of sending commands to the ESC.

Rotor RPM measurements were made with Eagle Tree brushless motor RPM sensors. These sensors tap into the motor power leads and provide a sinusoidal output voltage signal with a frequency equal to the commutation frequency of the motor. All of the motors used for this test are 7-pole motors, with a commutation frequency of 7 times the rotation speed. The LabVIEW program mentioned above provides filtering on the signal and uses a Fast Fourier Transform (FFT) to isolate the commutation frequency and record rotation speed for each motor. Based on the resolution of the FFT as well as comparison with a handheld optical tachometer during test preparations, the accuracy of

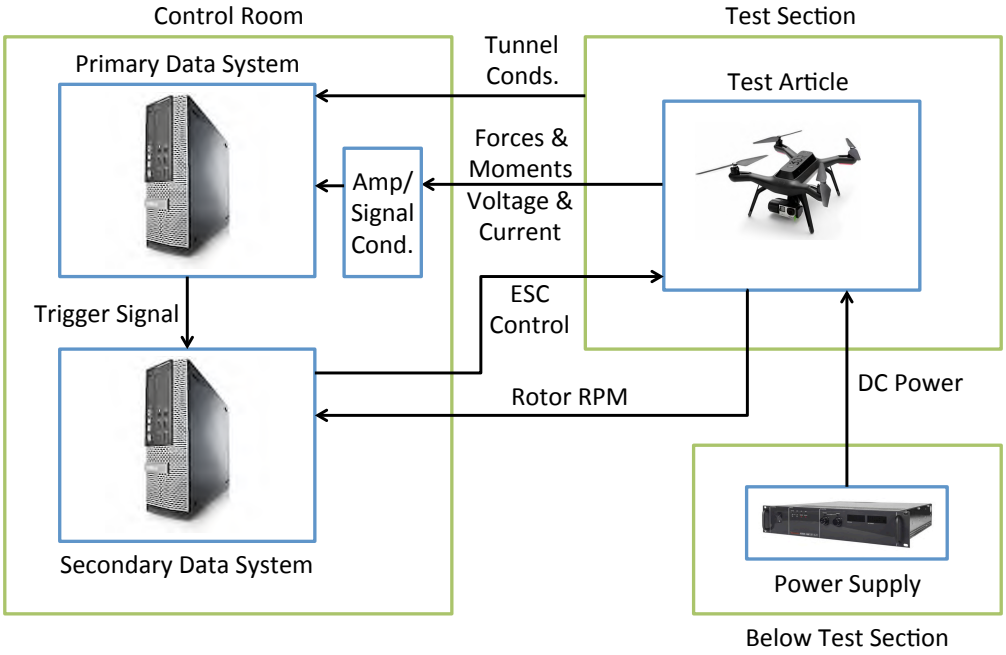

Figure 8. Schematic of data acquisition, control, and power systems.

the RPM measurements was estimated to be ±30 rpm. A typical operating rotor speed for the vehicles tested here is around 5,000 rpm, so the relative accuracy of the RPM measurements is better than ±1%. Acquisition of the motor RPM data was triggered by a signal from the primary data system so that the data collected by both systems was properly synchronized.

The forces and moments were measured using six-axis load cells manufactured by JR3, Inc. The majority of testing was carried out using a JR3 50-lb six-axis load cell, which has maximum loads of 50 lb in the x- and y-directions, 100 lb in the z-direction, and maximum moments of 150 in-lb in all three directions. Manufacturer-stated accuracy of the load cells is 0.25% of full-scale. Sting balances typically have accuracies no worse than 0.1% of full-scale, so some accuracy was sacrificed in favor of lower cost and hardware risk. Measurement uncertainty is addressed later in the Results section. The test plan originally called for a smaller 10-lb load cell for the lighter quadcopters, but early testing revealed significant vibrations that exceeded the capacity of the 10-lb load cell. The 50-lb model was therefore used for all five vehicles. These vibrations will be discussed later in the results section.

Mounting and interface hardware

Each test vehicle was installed using the "sting stand" as shown in Figs. 2-7. In order to expedite pitch movement using existing wind tunnel hardware and control systems, the vehicles were installed at a 90-degree right roll angle, allowing the tunnel turntable to be used to vary the vehicle angle of attack. This allowed parameter sweeps with arbitrary values of angle of attack without requiring access to the model. Changing the model yaw angle required manual adjustment, but only a handful of yaw angles were tested per vehicle, so making yaw angle changes did not have a significant impact on testing time.

The hardware used to mount the vehicles on the sting stand allowed quick model changes by using an interface that was common to all five multicopters. A drawing of the mounting hardware is shown in Fig. 9 and a close-up photograph of the mounting hardware is shown in Fig. 10. Note that the viewing angle is flipped 180 degrees between Figs. 9 and 10 to show the details of the hardware. Also shown in both images are the directions of the forces measured by the load cell and the direction of airflow relative to the model. The forces were measured using typical aircraft body axes, with F_x positive downstream, F_z positive up, and F_y positive to the right. Moments were defined as M_x positive roll right, M_y positive nose up, and M_z positive nose right. Again, the model is mounted at a 90 deg roll angle, so the y- and z-directions of the load cell do not align with a typical wind tunnel coordinate system.

The yellow sting attachment bar parallel to the x-axis in Fig. 9 was inserted into the sting tube on the sting stand and was bolted in place for the duration of the test. The load cell is shown in gray, and the model interface plates were bolted on top of the load cell as shown. Each model has its own mounting plate with a 1.25-inch-diameter boss that inserted into the interface plate and was secured in place with four bolts. Figure 11 shows an example model mounting plate. Because each model has the same 1.25-inch boss, model changes could be made very quickly during the test.

Yaw changes were made by rotating the yaw stub (shown in dark blue) below the load cell inside of the yaw tube, shown in orange. Two bolts could then be inserted into a series of threaded holes, allowing model yaw angles of 0, 5, 10, 30, 45, 60, and 90 deg.

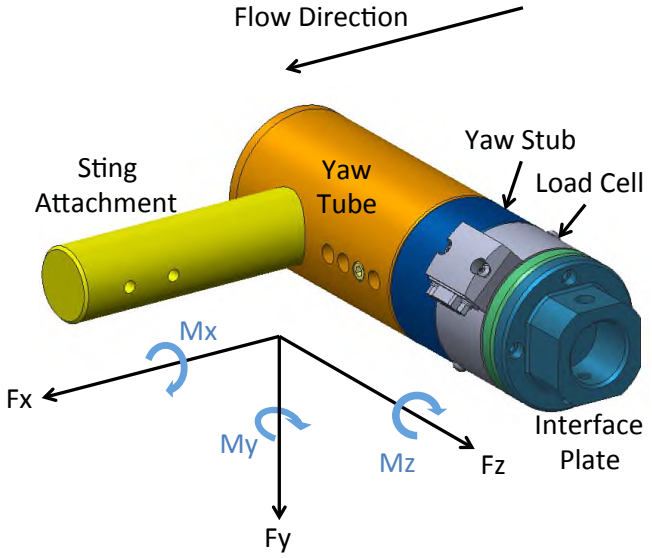

Figure 9. Model mounting hardware.

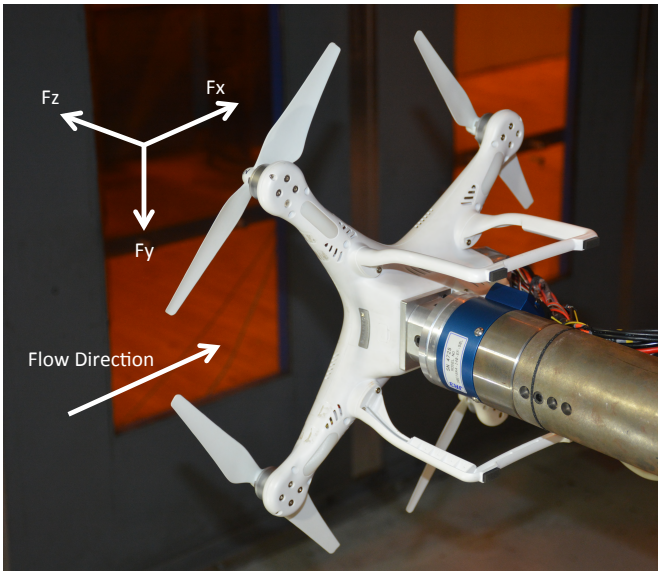

Figure 10. Close-up of DJI Phantom 3 mounted on sting stand.

Figure 11. Model mounting plate for DJI Phantom 3.

For the DJI and 3DR quadcopters, shown in Figs. 2-4, the camera gimbal mounting holes were used to support the vehicles and serve as attachment points to the interface hardware. The DAx8 octocopter (Fig. 5) and SUI Endurance quadcopter (Fig. 6) are heavier vehicles, so the camera mounting holes did not provide sufficient strength to support the vehicle weight and aerodynamic loads. For the latter two vehicles, the mounting hardware was attached directly to the vehicle chassis. For the Endurance, it was possible to attach the DJI Phantom mounting plate to the bottom chassis plate of the vehicle. For the DAx8, a set of metal struts had to be fabricated to attach to the vehicle inner structure as shown in Fig. 12.

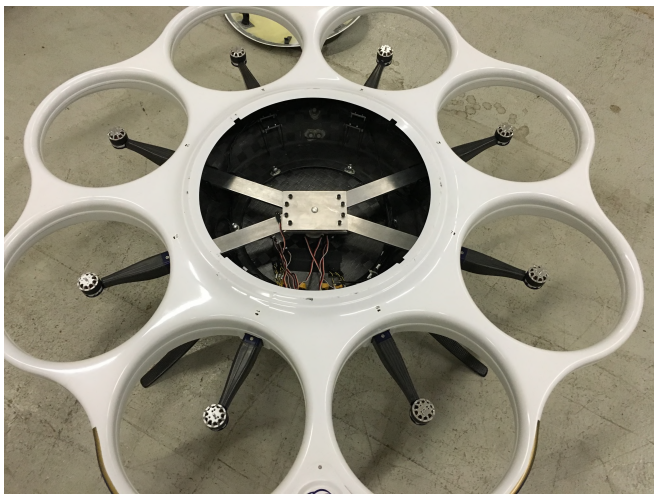

Figure 12. Drone America x8 internal mounting hardware.

Test matrix and testing procedures

For each model, the test plan called for three different configurations to be tested in the wind tunnel: full vehicle, bare airframe (rotors removed), and isolated rotor. By testing the vehicles in these three configurations, it will be possible to determine the performance of the rotors in isolation as well as the full vehicle performance, where rotor-to-rotor and rotor-to-airframe interactions have an effect. Additionally, the bare airframe runs will provide measurements of the forces and moments on the vehicle structure with the airframe drag being the primary measurement of interest.

In hover, both the full vehicles and isolated rotors were tested. Again, these measurements will make it possible to quantify the isolated rotor performance as well as the effects of aerodynamic interactions between the rotors and airframe.

Rotor RPM was varied in two ways for the full vehicle configurations. First, the rotor speed was changed uniformly for all of the rotors on the vehicle in order to quantify the effects of RPM on the vehicle forces and moments, particularly lift and drag. Second, non-uniform rotor speeds were tested, where there was a difference in RPM either from front to back or from side to side. These differential RPM runs will allow quantification of the pitch and roll moments that can be induced by the rotors as well as provide estimates of the different rotor speeds required to trim pitching moment in forward flight.

The primary variables for each test run were model angle of attack and rotor RPM. Each run started with a set of static and housekeeping points with wind off and wind on that were repeated at the end of the run to check for repeatability of measurements. To facilitate the application of aerodynamic tares, speed was set based on dynamic pressure, q. With speed and vehicle pitch fixed, RPM was swept from approximately 80 to 120 percent of the baseline RPM. All target rotor speeds were rounded to the nearest 100 rpm to make RPM adjustments easier. Baseline RPM was selected based on a thrust approximately equal to the manufacturers' specified nominal flight weight. Table 2 gives the baseline thrust and rotor speed for each of the five test vehicles.

Table 2. Baseline vehicle thrust and rotor RPM.

Vehicle	Baseline Thrust (lb)	Baseline Rotor RPM
3DR SOLO	3.3	5,700
3DR Iris+	2.8	5,400
DJI Phantom 3 Advanced	2.8	5,300
Drone America DAx8	12.8	7,000
SUI Endurance	6.0	3,500

RPM for each rotor was adjusted manually on the secondary data acquisition system as described earlier. After testing the uniform RPM data points, differential rotor speed was tested to measure moments on the vehicles. The procedure was then repeated for a series of pitch angles. The test matrix is summarized in Table 3 and presented in full in Tables A1-A3 in the Appendix. The bulk of testing concentrated on the full vehicle configurations at nominal speeds of 20 and 40 ft/s, with a limited number of runs at 60 and 80 ft/s. Due to time constraints, yaw sweeps as well as isolated rotor testing were limited to the 3DR SOLO, DAx8, and the SUI Endurance.

Table 3. Test matrix summary.

Configuration	Pitch (deg)	Yaw (deg)	Airspeed (ft/s)	RPM (% baseline)
Full Airframe	-40 – 40	0 – 90	20 – 80	80 – 120
Bare Airframe	-40 – 40	0 – 90	20 – 80	N/A
Rotor Only	-40 – 40	N/A	20 – 80	80 – 120
Hover	N/A	N/A	0	70 – 130

For the DAx8 and the Endurance, hover testing was done with the model mounted in the wind tunnel due to limited availability of those two vehicles. The remaining three vehicles were hover tested in a lab. In the wind tunnel, the rotors are approximately six feet from the walls, so there is potential for recirculating air to affect the measurements. In the lab, the models were mounted on the sting stand, with the nearest wall approximately 30 feet away. Recirculation should therefore not be a problem for the data collected in the lab. The effects of recirculation for the hover tests in the tunnel have yet to be quantified.

Data reduction and corrections

Most of the data processing was performed in real time by the BDAS system. The two post-processing tasks required were temperature drift corrections and application of aerodynamic tares. During the test, it was observed that the final static points were not matching well with the initial static points. In particular, the z-force for the final static point was often approximately 0.1 – 0.3 lb less than that for the initial static point on a given run. This drift appeared to be well correlated with temperature changes in the test section. After the test was completed, a linear fit was generated for each of the six force and moment measurements relating temperature change to drift in the static point force measurements. The z-force measurement drift with temperature is plotted in Fig. 13 along with the linear fit to the data.

The temperature typically increased from the beginning of a run to the end because testing was carried out in the morning and early afternoon when exterior temperatures were rising. As the plot shows, there is additional scatter in the data not related to temperature drift. This scatter can provide a first approximation of the uncertainty in the test measurements and is discussed further in the Measurement Uncertainty section.

The linear fit based on tunnel temperature was applied to the force measurements using the recorded temperature for each data point. The results of these corrections for an example run are shown in Fig. 14. The data shown are for the 3DR Iris+ at q = 1.9 lb/ft^2, with pitch ranging from -5 to 0 deg and RPM from 4,300 to 6,500, plus differential RPM. In this particular case, the temperature increased from 54.6° F at the beginning of the run to 62.9° F at the end of the run. This temperature change resulted in the uncorrected z-force measurement for the final static point being 0.2 lb below the initial static point reading, or about 4% of the maximum force measured during this run. After application of the temperature drift correction, the final static point only differs from the initial static point by 0.003 lb.

Load cell aerodynamic tares for the full vehicles and bare airframes were measured with just the model interface plate installed and taped over as shown in Fig. 15 (note that this photo was not taken in the wind tunnel, but does show the configuration as tested for the aerodynamic tares). Not

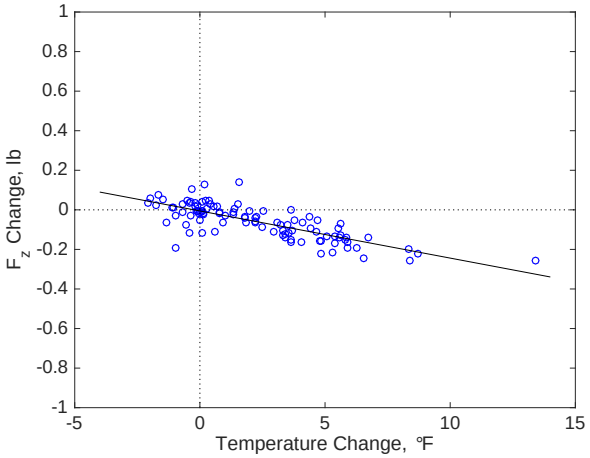

Figure 13. Variation of z-force static measurements with temperature.

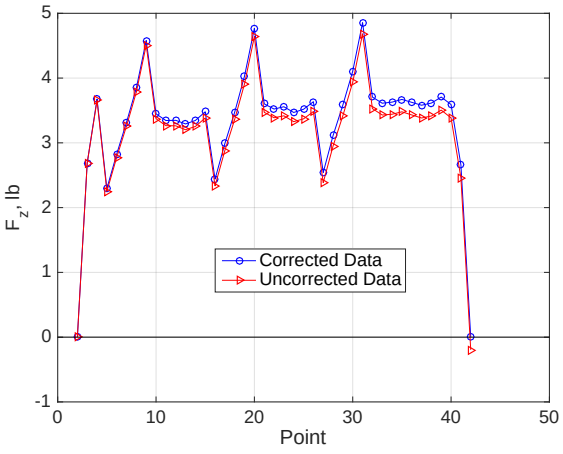

Figure 14. z-force for Run 63 – 3DR Iris+ with and without temperature drift corrections.

accounted for in the tares were the effect of the individual model mounting plates and the cables that supplied power and RPM commands to the vehicles. The mounting plates were not included, because putting them in the airstream in isolation would not be representative of their effects on the full model. The cables were not included, because with the vehicle removed, there was nothing to attach them to. A separate set of aerodynamic tares was measured for the isolated rotors, and this configuration is shown in Fig. 16. For the isolated rotor tares, all of the hardware shown in Fig. 7 was installed except for the rotor blade.

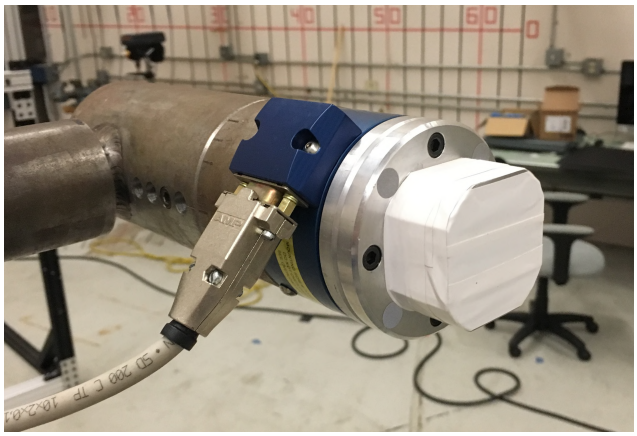

Figure 15. Full vehicle and bare airframe aerodynamic tare configuration.

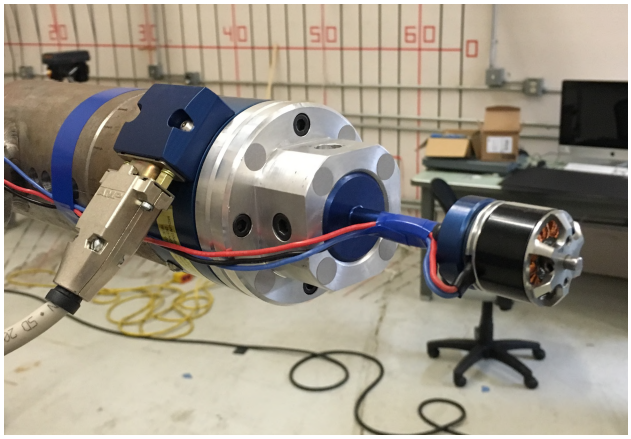

Figure 16. Isolated rotor aerodynamic tare configuration.

Typically in this type of wind tunnel test, weight tares would be required to account for changes in the model center of gravity relative to the load cell during model pitch changes. For this test, however, weight tares were not required, because the model was mounted on its side and the load cell moved with the model. In this configuration, the gravity vector of the model does not move relative to the load cell during pitch changes. The gravity vector does move relative to the load cell for model yaw changes, but a new data run was started any time the model yaw was changed, at which point the load cell measurements were re-zeroed.

RESULTS

A selection of the test results is presented in this section. A follow-on data report will be published containing additional data. Forward flight results for the full airframes will be presented first in this section including trim analysis, followed by bare airframe and isolated rotor results. Next, a subset of the hover test results will be presented. The vibrations of the models will then be discussed, followed by a discussion of measurement uncertainty.

Full Airframe

Lift and drag results for all five vehicles are presented in Figs. 17-26. For the three smaller quadcopters (Figs. 17-22), the scales on the lift and drag plots are the same in order to show any differences between these similar vehicles. Test conditions shown include variations in RPM and model pitch at zero degrees yaw and q = 0.48 lb/ft^2 (approximately 20 ft/s). For the 3DR SOLO and SUI Endurance, pitch angles were tested from -40° to +40° (positive pitch defined as nose-up) at this airspeed. DAx8 pitch ranged from -40° to +20°. Due to time constraints, positive angles of attack were not tested for the DJI Phantom or 3DR Iris+, with pitch ranging from -40° to 0°.

In general for the quadcopters, lift increases from " = -40° to 0° and then levels off. For the DAx8 octocopter, lift continues to increase above zero pitch, most likely because the DAx8 airframe generates a significant amount of lift at positive angles of attack. For all five vehicles, the drag increases monotonically with angle of attack. This is not surprising, since at negative angles of attack, the rotors are thrusting forward, and at positive angles of attack, they are thrusting aft.

The variation in drag with rotor RPM at zero angle of attack is not consistent across the five different vehicles. The DAx8 shows the largest dependence of drag on RPM, with the drag almost doubling as RPM is increased from the lowest to the highest rotor speed. For the other vehicles, this variation is much less pronounced at zero pitch. The cause of this discrepancy is yet to be determined, but may be aerodynamic interactions or differences in rotor geometries.

Trim

By searching for the regions where the lift values equal the weight of the vehicle and where the net drag force and pitching moment are zero, it is possible to estimate at what RPM and pitch value the trim condition is reached. Figure 18 shows that for all rotor speeds, the drag values for the SOLO pass through zero at approximately " = -6°. At " = -6°, the RPM for a lift value of 3.3 lb (the nominal flight weight of the SOLO including camera and battery), is approximately 5,400 rpm.

To trim moments, a higher rotor speed would be required on the aft rotors. Pitching moment for the differential RPM runs with the SOLO at q = 0.48 lb/ft^2 is shown in Fig. 27. The

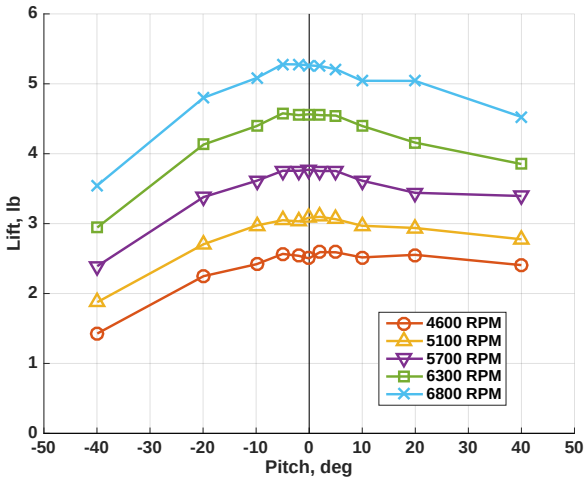

Figure 17. Lift for 3DR SOLO, q = 0.48 lb/ft^2, yaw = 0°.

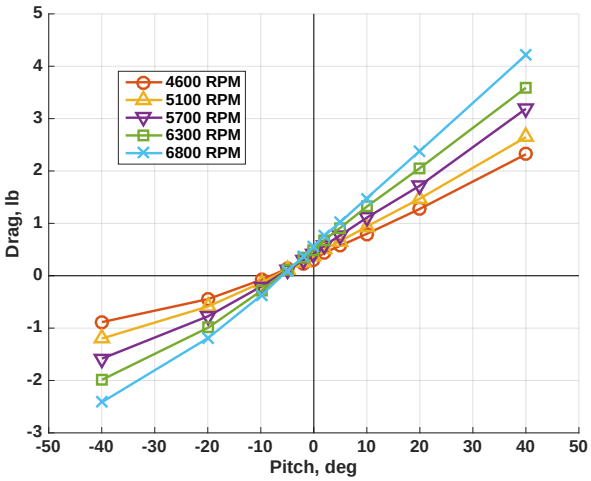

Figure 18. Drag for 3DR SOLO, q = 0.48 lb/ft^2, yaw = 0°.

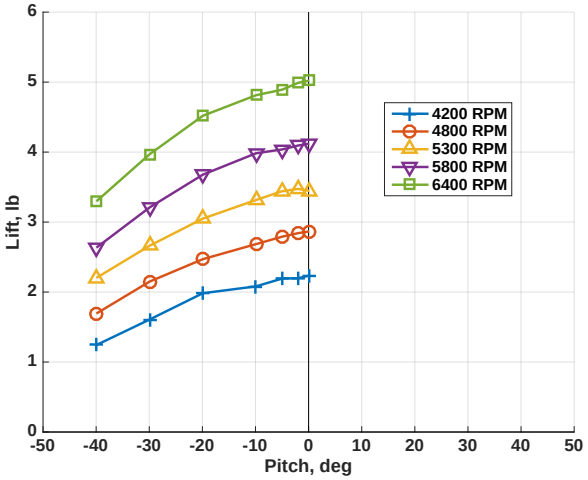

Figure 19. Lift for DJI Phantom 3, q = 0.48 lb/ft^2, yaw = 0°.

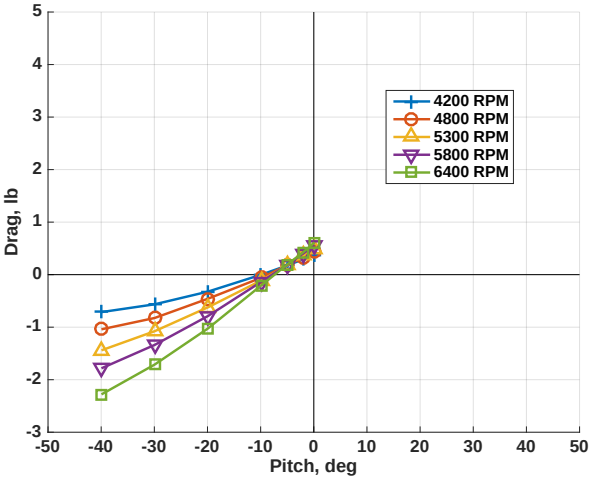

Figure 20. Drag for DJI Phantom, q = 0.48 lb/ft^2, yaw = 0°.

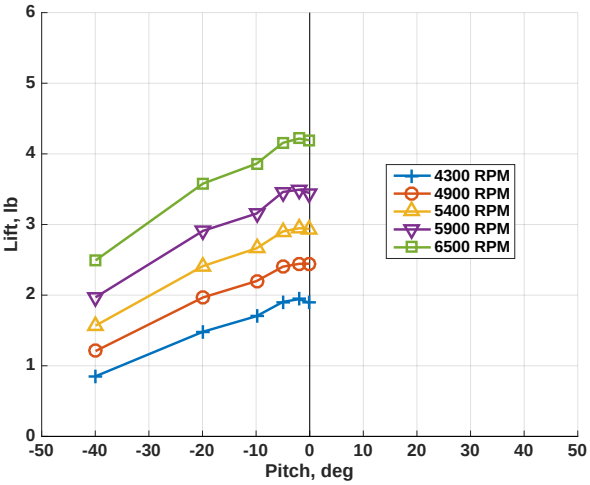

Figure 21. Lift for 3DR Iris+, q = 0.48 lb/ft^2, yaw = 0°.

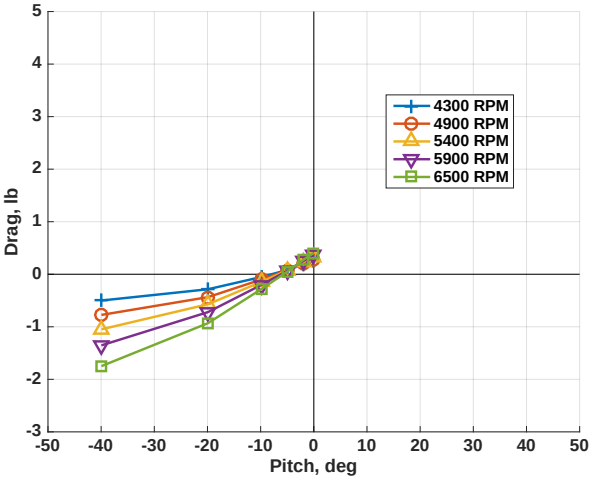

Figure 22. Drag for 3DR Iris+, q = 0.48 lb/ft^2, yaw = 0°.

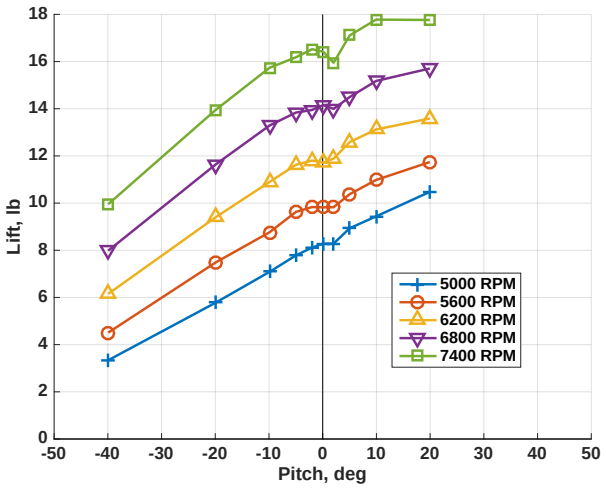

Figure 23. Lift for DAx8, q = 0.48 lb/ft^2, yaw = 0°.

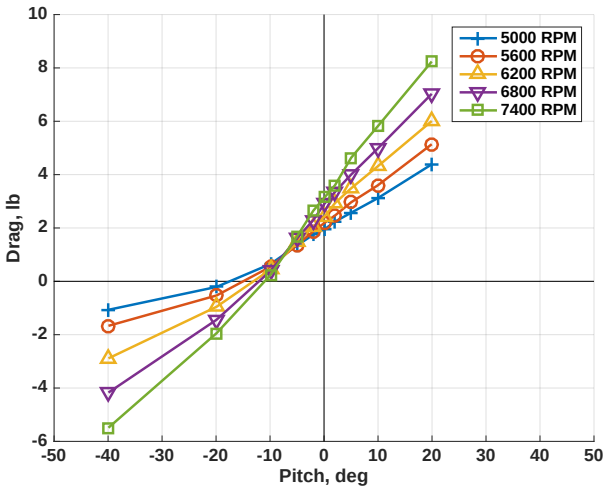

Figure 24. Drag for DAx8, q = 0.48 lb/ft^2, yaw = 0°.

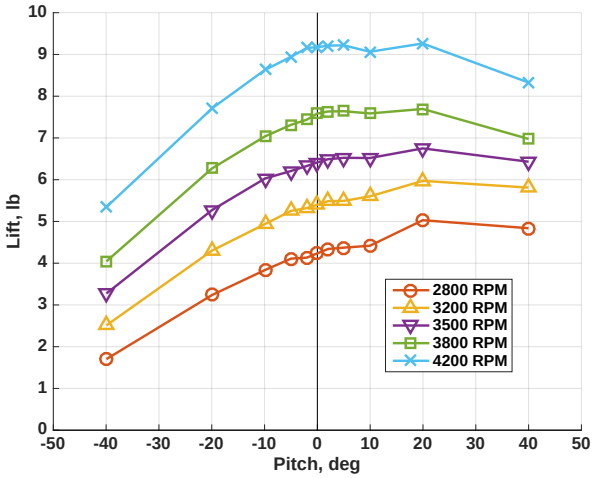

Figure 25. Lift for SUI Endurance, q = 0.48 lb/ft^2, yaw = 0°.

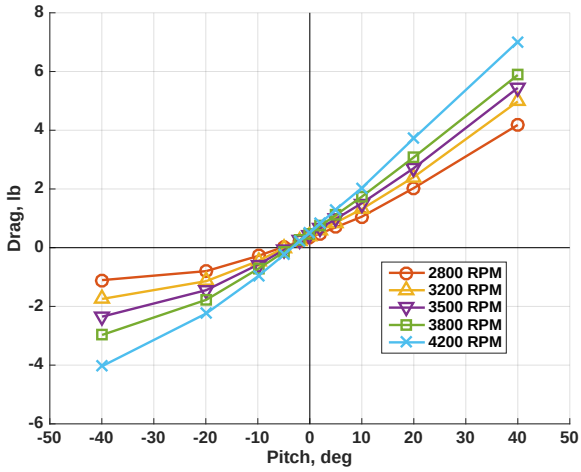

Figure 26. Drag for SUI Endurance, q = 0.48 lb/ft^2, yaw = 0°.

moments are expressed about a point at the center of the four rotors at the height of the rotor plane. Based on Fig. 27, at " = -6°, a pitch moment of zero would be reached for a rotor speed of approximately 6,200 rpm on the aft rotors and 5,200 on the forward rotors. Assuming changes in pitching moment are only dependent on the difference in rotor speeds (and not on the average rotor speed, which is not a bad approximation), the trim condition for the SOLO at q = 0.48 lb/ft^2 would be a pitch of -6°, forward rotor RPM of 4,900 and aft rotor RPM of 5,900.

Bare Airframe

Lift and drag results for the bare airframe runs are shown in Figs. 28 and 29. The solid lines show results for q = 1.9 lb/ft^2 (40 ft/s), and the dotted lines show results for q = 0.48 lb/ft^2 (20 ft/s). The results are shown normalized by dynamic pressure to expose any Reynolds number effects. The quadcopter airframes all generate very little lift. The DAx8

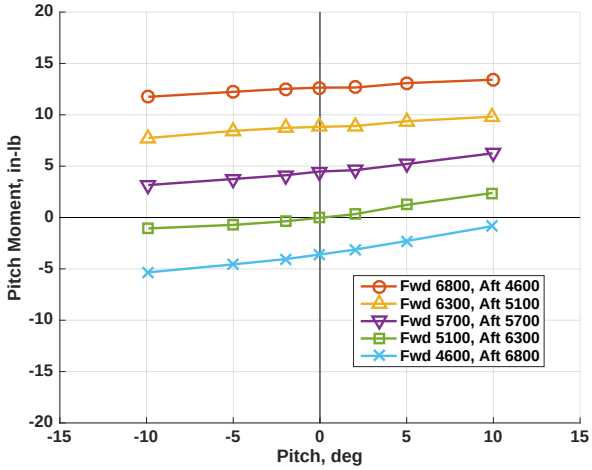

Figure 27. Pitching moment for the 3DR SOLO, q = 0.48 lb/ft^2, yaw = 0°, differential RPM.

octocopter airframe, however, is a large flat disk with a curved top, so it actually does generate a significant amount of lift. The curves for the two airspeeds are very similar, indicating very little effect of Reynolds number on lift.

Because the DAx8 is a much larger vehicle than the quadcopters, its drag is much higher and makes it difficult to interpret the results for the smaller vehicles in Fig. 29. The same drag results are shown in Fig. 30 but with the DAx8 results removed to increase the scale and better show the quadcopter results. The Reynolds number effects on drag of the DAx8 and SUI Endurance airframes are minimal. For the smaller quadcopters, lowering the speed results in a higher q-normalized drag.

Isolated Rotor

In addition to the full airframe runs, the isolated rotors of the 3DR SOLO, DAx8, and SUI Endurance were tested in forward flight. This configuration was previously shown in Fig. 7 for the SUI Endurance rotor. A small metal adapter was fabricated to attach a motor to the model interface plate with a standoff distance of 2.1 in from the interface plate. The adapter only allowed for attaching a motor with a 16 mm x 19 mm bolt pattern (the standard bolt pattern used by the motors on the Iris+, SOLO, and Phantom 3). Therefore, an Iris+ motor was used for all of the isolated rotor tests. Due to time constraints on testing, only a limited number of conditions were tested for the isolated rotor cases. These conditions are listed in Table A3 in the Appendix. Figures 31 and 32 show the lift and drag for the 3DR SOLO rotor at q = 0.48 lb/ft^2.

By comparing the isolated rotor results with the full airframe results, it is possible to estimate the effect of rotor-airframe and rotor-rotor interactions. For example, at 0 degrees pitch and 5700 RPM, the isolated rotor generates 1.0 lb of lift. For the same test condition with the full airframe, the lift shown in Fig. 17 is 3.8 lb, and the bare airframe lift (calculated by multiplying the value given in Fig. 28 by 0.48 lb/ft^2) is 0.01 lb. With no aerodynamic interactions, the total expected lift would be the number of rotors (4) times the isolated rotor lift, plus the isolated airframe lift, for a total of 4.01 lb. This indicates that at q = 0.48 lb/ft^2 and zero pitch, approximately 5 percent of the SOLO rotor lift is lost to rotor-airframe and rotor-rotor interactions. Similar calculations can be made for the other vehicles and different test conditions.

Because there are no flap hinges on the rotors used for these small vehicles, it can be expected that the rotors will carry hub moments, especially at higher airspeeds. As an example, the roll moment at the SOLO rotor hub at q = 0.48 lb/ft^2 is given in Figs. 33 and 34, first as the measured roll moment, and second as the lift offset. The lift offset is given by:

$$Offset = \frac{M_x}{F_z R}$$

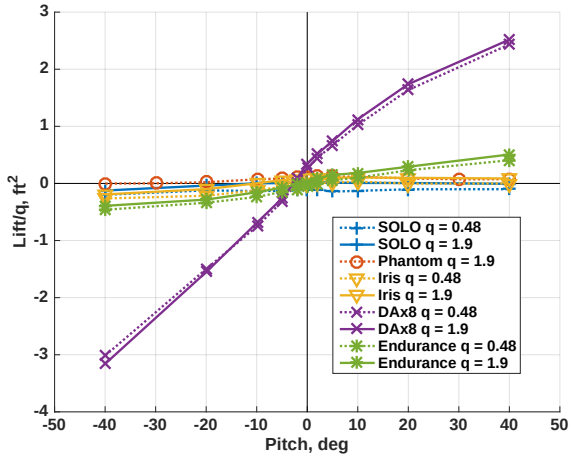

Figure 28. Lift/q for bare airframe runs.

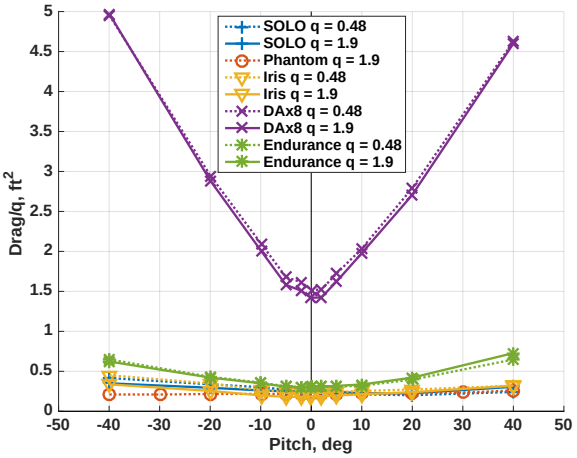

Figure 29. Drag/q for bare airframe runs.

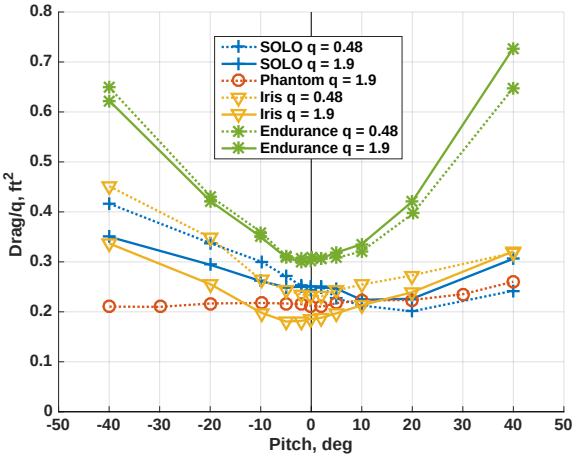

Figure 30. Drag/q for bare airframe runs (DAx8 results removed).

Roll moment varies much more with shaft pitch than with rotor RPM. The lift offset peaks at a pitch angle of -2° for all rotor speeds and varies from 5 to 8 percent of the rotor radius. As expected, the lift offset generally decreases with increased rotor speed (and decreased advance ratio). Advance ratios range from 0.07 at 6,800 RPM to 0.10 at 4,600 RPM. It is unclear why the lift offset is higher for 5,100 RPM than it is for 4,600 RPM; however, it could be due to measurement error, since the measured roll moments are very small. The discrepancy could be due to Reynolds number effects.

For q = 1.9 lb/ft^2 (not shown), the measured lift offset was as high as 13% for an RPM of 5,700; however, a resonance issue encountered with the test stand prevented testing the two lower rotor speeds at this higher airspeed.

Finally, isolated rotor tests enable measurement of individual rotor shaft torque, allowing calculation of the mechanical power produced by the rotor at each test condition. Results for both mechanical and electrical power are given in Fig. 35 for the 3DR SOLO rotor at q = 0.48 lb/ft^2. The motors and ESCs have not yet been bench tested for their individual efficiencies, so dividing the value for the mechanical power (solid line) by the electrical power (dotted line) gives the electrical efficiency of the combined motor and ESC. In this case the efficiency is between 72 and 78 percent, depending on rotor speed. Note that a motor and ESC from the 3DR Iris+ were used for all three isolated rotors that were tested. As the results in Fig. 35 show, the power is largely independent of shaft pitch angle, and is much more dependent on rotor RPM. The results for the other two isolated rotors tested (not presented here) showed similar trends.

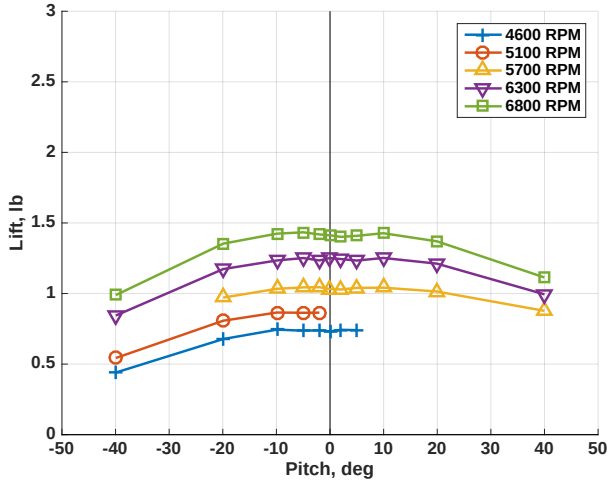

Figure 31. Lift for 3DR SOLO rotor, q = 0.48 lb/ft^2.

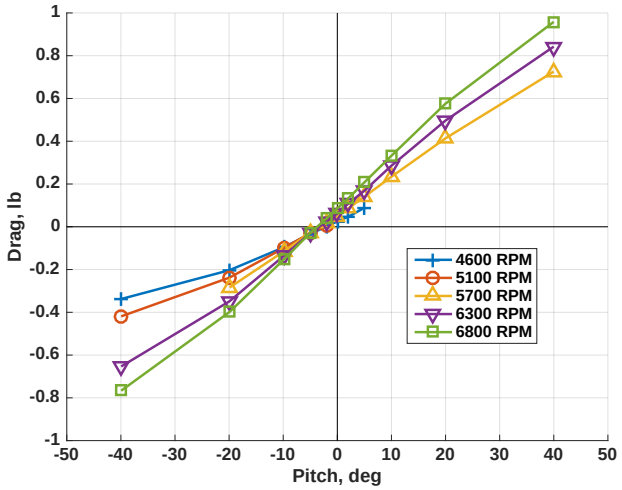

Figure 32. Drag for 3DR SOLO rotor, q = 0.48 lb/ft^2.

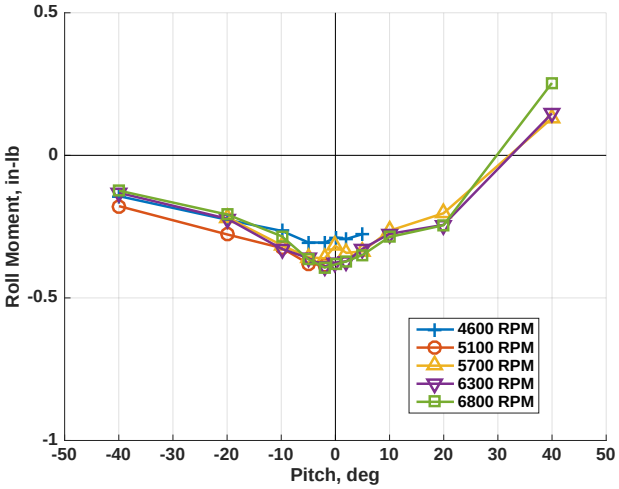

Figure 33. Roll moment for 3DR SOLO rotor, q = 0.48 lb/ft^2.

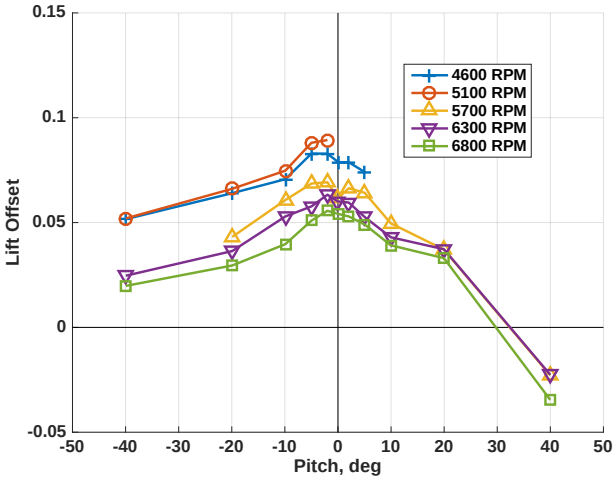

Figure 34. Lift offset for 3DR SOLO rotor, q = 0.48 lb/ft^2.

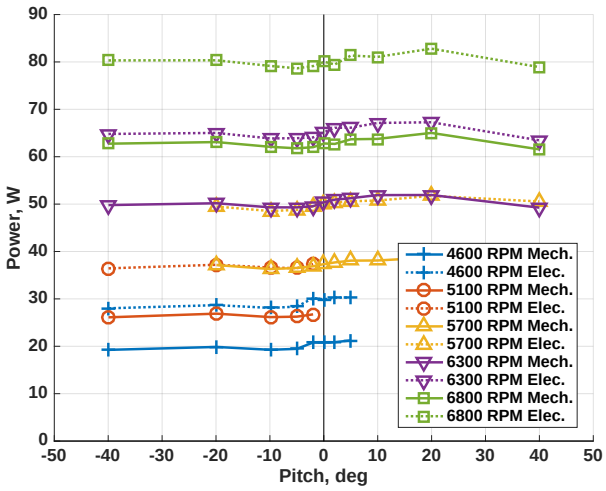

Figure 35. Power for the 3DR SOLO rotor, q = 0.48 lb/ft^2.

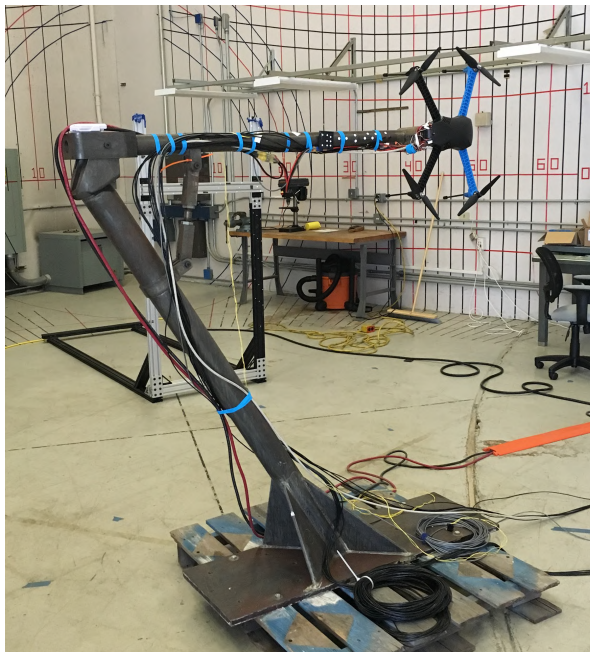

Figure 36. 3DR Iris+ hover test configuration.

Hover Test Results

The hover performance was measured for all five complete vehicles and all five isolated rotors. As previously mentioned in the Test Description section, the DAx8 and SUI Endurance were hover tested in the test section of the 7- by 10-ft wind tunnel mounted at zero degrees in the wind-on test configuration. The remaining three vehicles and all five isolated rotors were tested on the sting stand in a lab, as shown in Fig. 36. A clone of the BDAS system used in the wind tunnel was used for data acquisition in the lab. The range of hover test conditions is included with the full airframe and isolated rotor test matrices in Tables A1 and A3.

Results for the full vehicle hover tests are given in Figs. 37 and 38. The first figure shows the thrust as a function of rotor RPM and the second shows the thrust coefficient, defined as $T/\rho A(!\ R)^2$. As expected, the thrust follows a quadratic trend with rotor speed. Thrust coefficient for all five vehicles shows a slight increase with RPM, and the Phantom operates at the highest thrust coefficient of the five vehicles. The variation with rotor RPM indicates that non-dimensional rotor lift increases slightly with increasing Reynolds number over the range of rotor speeds tested. For reference, the Reynolds number at the tip of the DJI Phantom rotor blade at 5,000 RPM is approximately 50,000.

Thrust coefficient results for the isolated rotors are given in Fig. 39. The results are similar to the full vehicle results, but there is more noise in the thrust coefficient curves. This is likely due to higher relative measurement uncertainty for the isolated rotors. The thrust being measured is only a quarter of that of the full vehicles for the quadcopters (and an eighth of that of the octocopter), so the relative error in the measurement is four times higher, which carries into the thrust coefficient calculation. Regardless, the same trend is observed as for the full vehicle, with thrust coefficient increasing slightly with RPM.

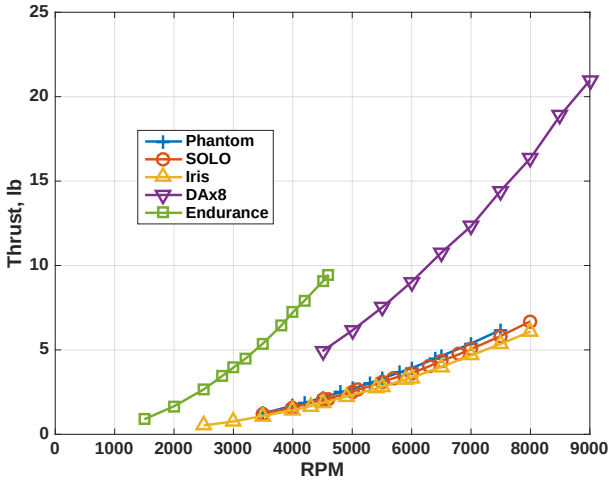

Figure 37. Full vehicle hover thrust.

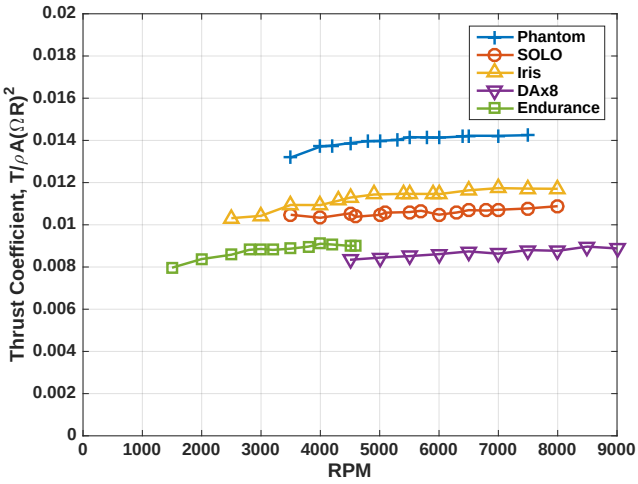

Figure 38. Full vehicle hover thrust coefficient.

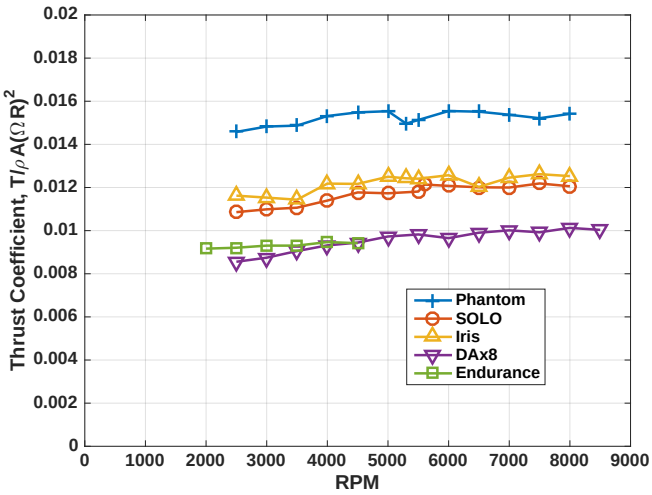

Figure 39. Isolated rotor thrust coefficient.

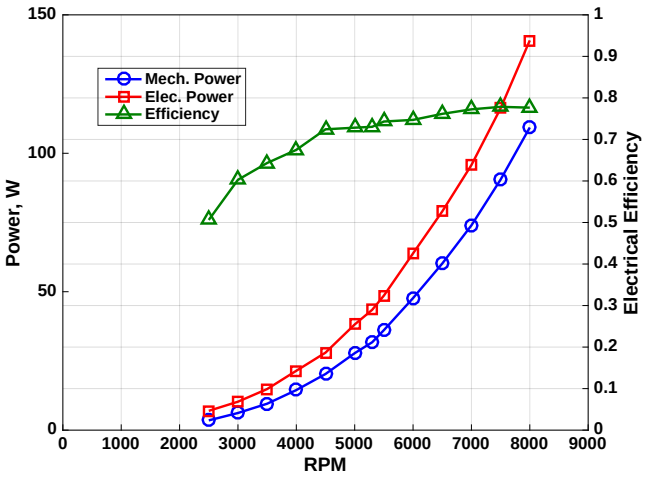

Figure 40. Hover power for DJI Phantom rotor.

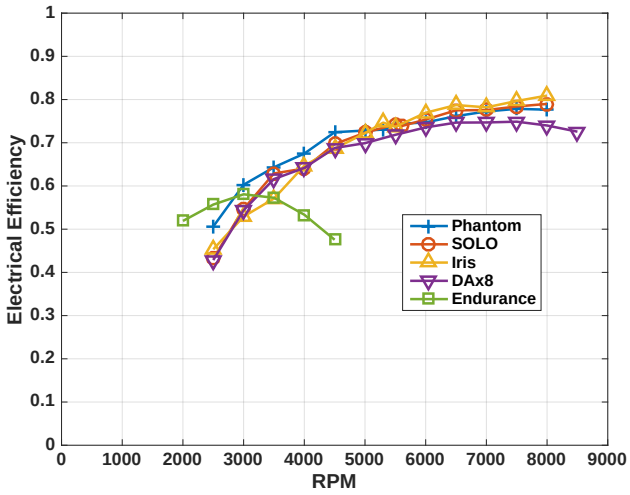

Figure 41. Isolated rotor electrical efficiency.

By comparing the full vehicle and isolated rotor results for thrust coefficient, it is also possible to calculate the download, *DL*, in hover with the following:

$$DL = \frac{C_{T,IR} - C_{T,FV}}{C_{T,IR}}$$

where the *IR* and *FV* subscripts represent isolated rotor and full vehicle, respectively. The hover download across all five vehicles for the baseline rotor speed ranges from a low of approximately 5% for the SUI Endurance to about 15% for the DAx8. The SUI Endurance has fairly thin arms supporting the rotors, while the DAx8 rotor support arms are relatively thick, which is likely the driving factor behind the difference in hover download between the different vehicles.

As with the forward flight isolated rotor tests, the mechanical and electrical power can be compared to compute the efficiency of the motor-ESC combination. The same motor and ESC from the Iris+ that were used for forward-flight testing were used for the hover tests. As an example, Fig. 40 shows the mechanical and electrical power of the DJI Phantom rotor on the primary y-axis. Electrical efficiency is plotted on the secondary axis. The combined motor-ESC efficiency is as low as 50% at the lowest RPM tested and increases quickly above 70% once rotor speed is increased to 4,500 rpm. Maximum efficiency of 77% was reached at the highest rotor speed tested. Efficiency results were similar to the Phantom results for the other similarly sized quadcopter rotors (3DR Iris+ and 3DR SOLO).

For the DAx8 and SUI Endurance, which use larger rotors, the efficiency drops off significantly, as shown in Fig. 41. Again, the Iris+ motor was used to test all five isolated rotors, and it was very under-sized for the larger rotors. This is particularly true for the 15-inch SUI rotor, which is normally mated to a much larger motor on the vehicle. The highest electrical efficiency for the isolated rotor hover tests was measured for the Iris+ rotor, which is not surprising, since the motor and rotor are normally paired to achieve maximum efficiency on the production vehicles. If the other rotors were hover tested with their appropriate motors, the measured electrical efficiencies would be expected to be higher.

Finally, with the mechanical power and thrust measurements, it is possible to calculate the rotor figure of merit, *M*, defined as the ratio of ideal induced power to total rotor mechanical power:

$$M = \frac{T\sqrt{T/2\rho A}}{P_{mech}}$$

In the above equation, T is the rotor thrust, and P_{mech} is the mechanical power, equal to M_z! . The measured figure of merit for all five rotors is plotted in Fig. 42. The highest figure of merit measured is for the 3DR Iris+, which has a maximum of 0.72 at 8,000 rpm. For each rotor, the figure of merit is maximized at the upper end of the RPM range. The

results show good agreement with results from Ref. 6 for the APC Thin Electric 10x5 blade, which has a similar geometry to the rotors of the DJI Phantom 3. The figure of merit for the APC blades ranges from 0.59 at 2,508 rpm to 0.66 at 6,708 rpm, while for the Phantom blade measured here, the figure of merit is 0.58 at 2,500 rpm and 0.67 at 6,500 rpm.

The four smaller quadcopter rotors have very similar trends for figure of merit. The SUI Endurance rotor has a higher figure of merit at the low RPM values than any of the other rotors. The Endurance rotor was limited to a maximum speed of 4,500 rpm because of the power limit of the Iris+ motor being used for isolated rotor testing.

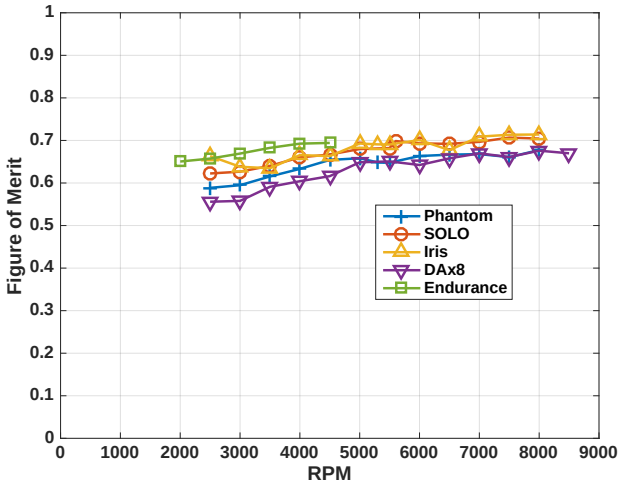

Figure 42. Isolated rotor figure of merit.

Vibrations

One of the initial challenges encountered during the wind tunnel test was a high level of vibration. Vibrations in this type of vehicle are not unexpected, and in fact, the designs for all of the vehicles show that the manufacturers actively worked to reduce vibrations by using rubber dampers on critical components, the camera gimbals in particular. The level and character of vibration, however, was previously not well documented.

As discussed in the Test Setup section, the BDAS system was configured to measure the mean values of the load cell measurements over a 30-second data record. It was not set up to measure dynamic data; however, the signal conditioning/amplifier system could be used at any time to capture short data records at a rate of 100,000 samples per second. Vibration data were collected for several test points using this system. Sample results for the 3DR SOLO are provided in this section. Figure 43 shows a 0.5 second time history of F_x for the full vehicle for a rotor speed of 5,700 rpm at a vehicle pitch of zero degrees and q = 1.9 lb/ft^2 (approximately 40 ft/s).

At this condition, the mean drag is 0.8 lb, but as the plot shows, the peak loads are as much as ±10 lb. Additionally, due to the inconsistent phasing of the four rotors, the vibration magnitude varies significantly with time. If the plot showed a longer sample time, the beat frequency would be much more apparent. An FFT of the same data is given in Fig. 44.

At 5,700 rpm, the 1/rev frequency is 95 Hz. There is a low peak at 1/rev due to blade imbalance, but the primary vibration frequencies are at 2/rev and 4/rev. The 2/rev is explained by the fact that the rotors are 2-bladed, with very little flexibility in the lag direction. The alternating aerodynamic conditions seen by the blades between the advancing and retreating sides therefore lead to high 2/rev vibrations. Aerodynamic interactions between the forward and aft rotors are the likely cause of the higher harmonic content at 4/rev and 8/rev.

Vibrations were measured for the same test condition for the isolated rotor, and the results are shown in Fig. 45. Because there was only one rotor operating at a fixed speed, there is no beating as there is for the full vehicle results. Looking at

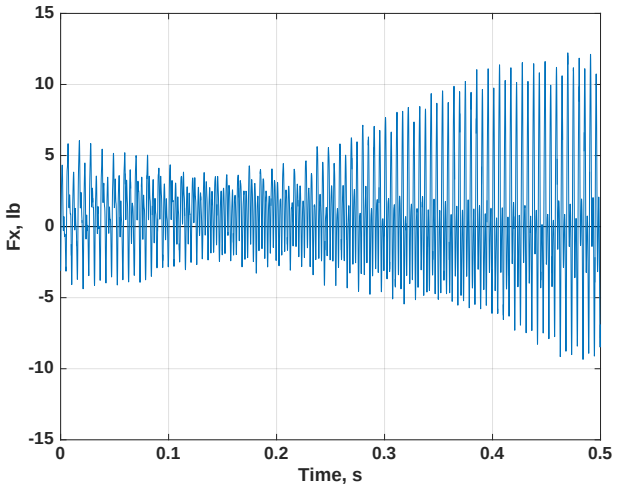

Figure 43. F_x time history for 3DR SOLO, q = 1.9 lb/ft^2, α = 0°, RPM = 5,700.

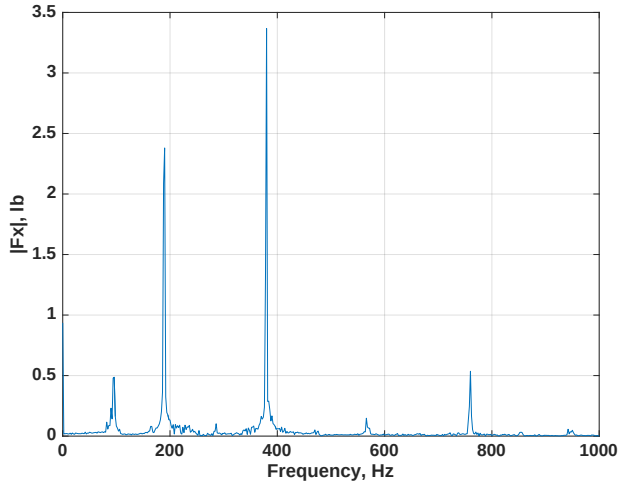

Figure 44. FFT of F_x for 3DR SOLO, q = 1.9 lb/ft^2, α = 0°, RPM = 5,700.

the FFT for the isolated rotor results, shown in Fig. 46, the highest vibration levels are at the 2/rev frequency, but there is still a significant amount of 4/rev content. Since the data shown here were collected at a shaft pitch of zero degrees, blade vortex interaction is the likely cause of the higher harmonic content [Ref. 15].

Because vibration measurements were not in the original test plan, there were only limited measurements taken. Further testing that focuses on better characterizing the vibrations of these vehicles and exploring mitigation strategies would therefore be a good follow-on topic of research.

Measurement Uncertainty

As previously mentioned, the manufacturer's stated uncertainty for the load cell is 0.25% of full scale. For the 50-lb load cell that was used for the majority of testing, the capacity in the x- and y-directions is 50 lb. In the z-direction, the capacity is 100 lb, and the moment capacity is 150 in-lb in all three directions. This translates to an uncertainty of 0.13 lb in the x- and y-force measurements, 0.25 lb in the z-force measurements, and 0.38 in-lb in all three moment directions. Based on the error analysis presented below, the uncertainty is believed to be less than the manufacturer's stated uncertainty for the load ranges measured during this test.

Check loads were performed both before and after the test in order to quantify the accuracy of the load cell over the load range tested. The results for the post-test check loads in the x-direction are shown in Fig. 47. Measurements were taken with both increasing and decreasing loads to check for hysteresis. If the load cell measurements were perfect, the measured loads would exactly follow the black line, with a slope of 1. The measured loads shown are slightly less than expected, with the absolute error increasing to a maximum of 0.19 lb as the load increases. The relative error for all of the check loads is fairly constant for the non-zero measurements, indicating that the slope of the sensitivity curve over this load range is slightly off. Based on the check load data, the uncertainty in the x-direction due to calibration error is calculated to be $\pm 0.020 F_x$. As shown, the hysteresis is very small, with a maximum value of 0.021 lb. The uncertainty in the x-direction due to hysteresis is therefore considered to be ±0.021 lb.

The third source of force and moment measurement uncertainty that can be applied across all of the data runs is the repeatability of measurements. Ideally, the temperature-corrected forces and moments measured for the static point at the end of each run would be zero; however, there is scatter in these ending static points (shown for the z-direction in Fig. 13). The 95% confidence interval for the uncertainty due to non-repeatability of data points is two times the standard deviation of the errors for the ending static points. The contributions to uncertainty for all six force and moment measurements are given in Table 4.

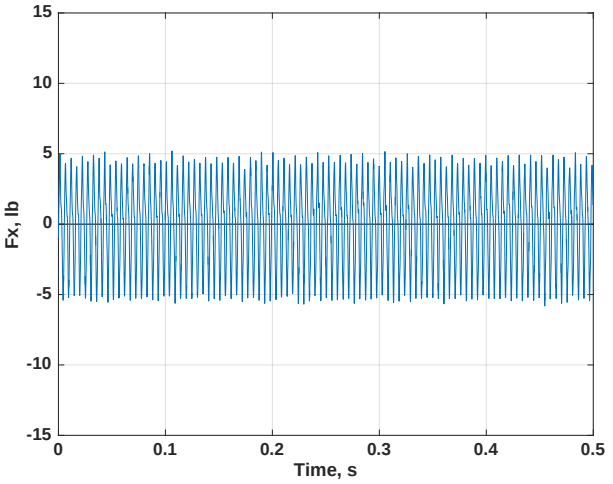

Figure 45. F_x time history for 3DR SOLO isolated rotor, q = 1.9 lb/ft^2, α = 0°, RPM = 5,700.

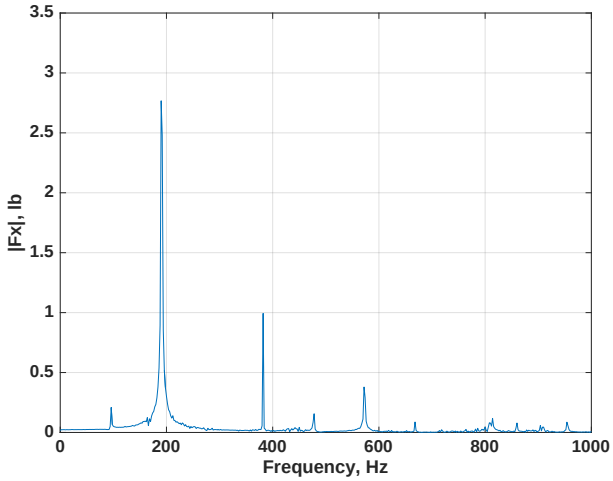

Figure 46. FFT of F_x for 3DR SOLO isolated rotor, q = 1.9 lb/ft^2, α = 0°, RPM = 5,700.

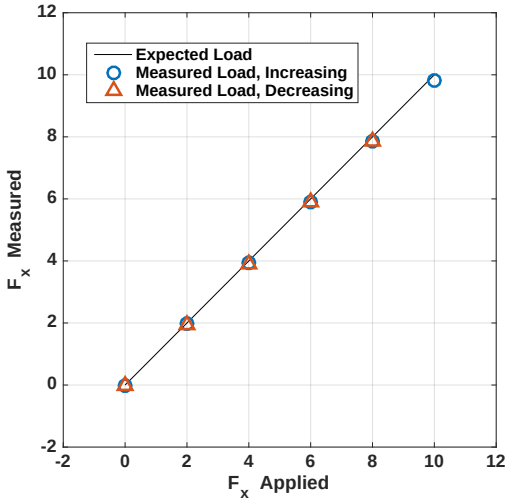

Figure 47. F_x check load results

The final source of uncertainty is the fact that the force and moment measurements are based on an average of unsteady loading measurements. For each measurement taken during the test, the standard deviation was recorded, so for a 95% confidence interval, the uncertainty due to measurement unsteadiness is $2\sigma/\sqrt{N}$, where σ is the standard deviation at a given data point and N is the number of samples. For the 30-second data records at 1,024 samples per second collected for this test, N equals 30,720.

The total measurement uncertainty is then calculated as the root-sum-squared of the four different uncertainty sources. Figure 48 shows an example of the z-force data with error bars for Run 63, which is the same run shown in Fig. 14. The maximum calculated uncertainty in the z-force for this run is 0.163 lb.

Table 4. Uncertainty contributions.

Source	F_x	F_y	F_z	M_x	M_y	M_z
Relative Cal. Error	0.020	0.012	0.002	0.004	0.003	0.008
Hysteresis, lb or in-lb	0.021	0.011	0.052	0.010	0.032	0.018
Repeatability, lb or in-lb	0.085	0.055	0.123	0.148	0.269	0.191

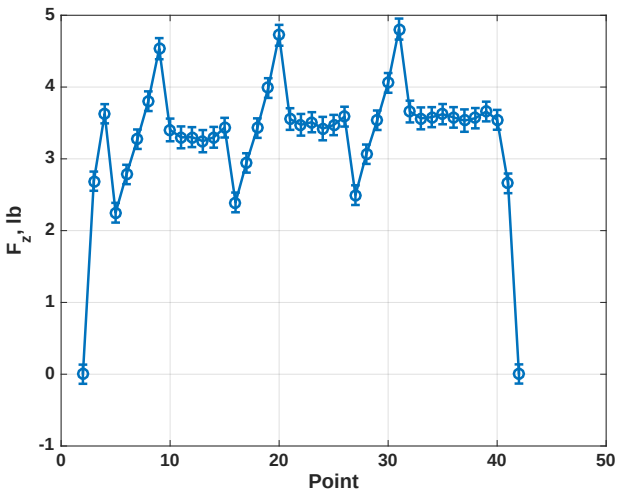

Figure 48. z-force for Run 63 – 3DR Iris+ including uncertainty.

FUTURE WORK

The next major research effort related to this test is to use the data to calibrate and validate the various models used to model multicopter vehicles. In particular, research under DELIVER and RVLT will seek to validate CAMRAD II models of small rotors using the data collected here. These models will then be used to calibrate rotor performance models in NDARC to allow for design trade studies of multicopter vehicles. Research under UTM will use the data collected here to help populate a vehicle performance database for multicopter vehicles. This database can then be used to accurately model trajectories of these types of aircraft. There is currently an effort underway to build a query-able database of the data collected in this test to make it easier to extract trends. In its current form, data can only be extracted by finding a desired test condition in the test log and pulling the matching data from the dataset.

There are also follow-on experimental efforts planned to further characterize small multicopter vehicles. The motors and speed controllers used for this test will be bench tested to better characterize their efficiency as a function of torque and motor RPM. These tests will follow the methodology described by Green and McDonald in Ref. 16. Finally, in order to accurately characterize the performance of these vehicles using a comprehensive analysis tool such as CAMRAD II, it may be necessary to measure blade deflections in flight. An effort is underway to use a photogrammetry system to measure the blade deflections in both hover and in forward flight.

CONCLUSIONS

The goal of this test was to generate a high-quality set of data for the performance of multicopter UAS vehicles. The intent is to use this data to enhance software tools in use both inside and outside of NASA to design and analyze multicopter vehicles. The applications targeted by this test are trajectory estimation and vehicle design and analysis, but there could certainly be others that will be able to make use of the data.

The test generated data for five different vehicles in both forward flight and in hover. The data include forces and moments and electrical power as a function of rotor RPM, airspeed, and vehicle attitude. This paper described the test setup and procedure as well as summarized the results of the test at a select number of operating conditions. A large amount of data from this test was not included in this paper and will be published in a technical report at a later date.

The data that were collected for the full vehicles as well as for the bare airframes and isolated rotors will allow for development and validation of analytical and numerical models at both the full vehicle and component levels. This breadth of validation data was previously unavailable in the public domain. The data produced by this research effort represent a significant step forward in advancing the understanding of multicopter UAS performance.

ACKNOWLEDGMENTS

A large team was required to accomplish this test, and the authors would like to acknowledge the contributions of all who were involved. In particular, the authors would like to thank Nili Gold and the 7- by 10-ft Wind Tunnel test crew for all the hard work they put in to ensure that the test ran smoothly. The NASA machine shop teams, led by Robert Kornienko and Vincent Derilo, produced the vehicle

mounting hardware, which was absolutely critical to the success of the test. Tom Norman provided invaluable insights into wind tunnel testing and data reduction. Straight Up Imaging provided the Endurance vehicle for the wind tunnel test. The assistance of all of those who acted as safety loads monitors during the test is greatly appreciated. Three NASA projects supported this test: the UAS Traffic Management (UTM) Sub-project, under the Safe Autonomous Systems Operations (SASO) Project; the Design Environment for Novel Vertical Lift Vehicles (DELIVER) Sub-project, under the Convergent Aeronautics Solutions (CAS) Project; and the Revolutionary Vertical Lift Technology (RVLT) Project.

REFERENCES

1. Gorton, S., López, I., and Theodore, C., "NASA Technology for Next Generation Vertical Lift Vehicles," AIAA SciTech, Kissimmee, FL, January 2015.

2. Johnson, W., "NDARC: NASA Design and Analysis of Rotorcraft," NASA/TP-2015-218751, April 2015.

3. Johnson, W., "Propulsion System Models for Rotorcraft Conceptual Design," AHS 5th Decennial Aeromechanics Specialists' Conference, San Francisco, CA, January 2014.

4. "UTM: Air Traffic Management for Low-Altitude Drones", NASA facts, NF-2015-10-596-HQ.

5. Brandt, J. and Selig, M., "Propeller Performance Data at Low Reynolds Numbers," 49th AIAA Aerospace Sciences Meeting, Orlando, FL, January 2011.

6. Brandt, J., Deters, R., Ananda, G., and Selig, M., "UIUC Propeller Data Site," http://m-selig.ae.illinois.edu/props/propDB.html, accessed March 28, 2016.

7. Carroll, T., George, I.-R., Bramesfeld, G., and Raahemifar, K., "Design Optimization of Small Rotors in Quad-Rotor Configuration," AIAA SciTech, San Diego, CA, January 2016.

8. Huang, H., Hoffmann, G., Waslander, S., and Tomlin, C., "Aerodynamics and Control of Autonomous Quadrotor Helicopters in Aggressive Maneuvering," 2009 IEEE International Conference on Robotics and Automation, Kobe, Japan, May 2009.

9. "SOLO Specs: Just the facts," https://3dr.com/solo-gopro-drone-specs/, accessed March 28, 2016.

10. "Phantom 3 Advanced Specs," http://www.dji.com/product/phantom-3-adv/info#specs, accessed March 28, 2016.

11. "3DR Iris+," https://3dr.com/iris-plus/, accessed March 28, 2016.

12. "Drone America – DAx8," http://www.droneamerica.com/systems/dax8, accessed March 28, 2016.

13. "Products – Straight Up Imaging," http://www.straightupimaging.com/products/, accessed March 28, 2016.

14. Storms, B., Nishikawa, D., Mason, S, Hange, C., and Phillips, J., "BDAS 13.2 User Manual," Rev. 2, February 2016.

15. Johnson, W., *Rotorcraft Aeromechanics*, Cambridge University Press, New York, NY, 2013, Chapter 18.3: Vibration, pp. 717-722.

16. Green, C, and McDonald, R. "Modeling and Test of the Efficiency of Electronic Speed Controllers for Brushless DC Motors," 15th AIAA Aviation Technology, Integration, and Operations Conference, Dallas, TX, June 2015.

Table A1. Full airframe test matrix.

Model	Speed (q, lb/ft^2)	Nominal Speed, ft/s	Yaw Angle, deg	Pitch Angle◆	RPM❖
3DR SOLO	0.48	20	0	-40 – 40	4,600 – 6,800 +Δ
	1.9	40	0	-40 – 40	4,600 – 6,800 +Δ
	7.7	80	0	-40 – -20	5,700 – 6,800
	0.48	20	-5	-40 – 40	4,600 – 6,800 +Δ
	1.9	40	-5	-40 – 40	4,600 – 6,800 +Δ
	1.9	40	-30	-10 – 10	4,000 – 6,300
	0.48	20	-45	-10 – 10	4,000 – 6,300 +Δ
	1.9	40	-45	-10 – 10	4,000 – 6,300
	1.9	40	-60	-10 – 10	4,000 – 6,300
	0.48	20	-90	-10 – 10	4,000 – 6,300 +Δ
	1.9	40	-90	-10 – 10	4,000 – 6,300
	0 (hover)	0	0	0	3,500 – 8,000 +Δ
DJI Phantom 3	0.48	20	0	-40 – 0	4,200 – 6,400 +Δ
	1.9	40	0	-40 – 0	4,200 – 6,400 +Δ
	0 (hover)	0	0	0	3,500 – 7,500 +Δ
3DR Iris+	0.48	20	0	-40 – 0	4,300 – 6,500 +Δ
	1.9	40	0	-40 – 0	4,300 – 6,500 +Δ
	0 (hover)	0	0	0	2,500 – 8,000 +Δ
Drone America x8	0.48	20	0	-40 – 20	5,000 – 7,400 +Δ
	1.9	40	0	-40 – 0	5,000 – 7,400 +Δ
	0.48	20	-5	-40 – 20	5,600 – 8,400 +Δ★
	1.9	40	-5	-40 – 0	5,600 – 8,400 +Δ★
	0.48	20	-30	-10 – 10	5,600 – 8,400★
	0.48	20	-45	-10 – 10	5,600 – 8,400 +Δ★
	0.48	20	-60	-10 – 10	5,600 – 8,400★
	0.48	20	-90	-10 – 10	5,600 – 8,400 +Δ★
	0 (hover)	0	0	0	4,500 – 9,000 +Δ
SUI Endurance	0.48	20	0	-40 – 40	2,800 – 4,200 +Δ
	1.9	40	0	-40 – 40	2,800 – 4,200 +Δ
	4.3	60	0	-40 – -20	4,200 – 5,000
	0.48	20	-5	-40 – 40	2,800 – 4,200 +Δ
	0.48	20	-30	-10 – 10	2,800 – 4,200
	0.48	20	-45	-10 – 10	2,800 – 4,200 +Δ
	0.48	20	-60	-10 – 10	2,800 – 4,200
	0.48	20	-90	-10 – 10	2,800 – 4,200 +Δ
	0 (hover)	0	0	0	1,500 – 4,600 +Δ

◆ Pitch angle is the angle of the tunnel turntable, so in terms of vehicle Euler angles, the pitch rotation would be executed first and the yaw angle second

❖ +Δ next to the RPM entries indicates that differential RPM values were tested in addition to the uniform RPM sweeps

★ During testing of the DAx8, the baseline RPM was changed from 6,200 to 7,000 to better represent the baseline weight of the vehicle

Table A2. Bare airframe test matrix.

Model	Speed (q, lb/ft^2)	Nominal Speed, ft/s	Yaw Angle, deg	Pitch Angle◆	RPM
3DR SOLO	0.48	20	0	-40 – 40	N/A
	1.9	40	0	-40 – 40	N/A
	7.7	80	0	-40 – 40	N/A
	0.48	20	-90	-10 – 10	N/A
	1.9	40	-90	-10 – 10	N/A
DJI Phantom 3	1.9	40	0	-40 – 40	N/A
3DR Iris+	0.48	20	0	-40 – 40	N/A
	1.9	40	0	-40 – 40	N/A
Drone America x8	0.48	20	0	-40 – 40	N/A
	0.48	20	0	-40 – 40	N/A
	0.48	20	-45	-10 – 10	N/A
	1.9	40	-90	-10 – 10	N/A
SUI Endurance	0.48	20	0	-40 – 40	N/A
	1.9	40	0	-40 – 40	N/A
	0.48	20	-90	-10 – 10	N/A

◆ Pitch angle is the angle of the tunnel turntable, so in terms of vehicle Euler angles, the pitch rotation would be executed first and the yaw angle second

Table A3. Isolated rotor test matrix.

Model	Speed (q, lb/ft^2)	Nominal Speed, ft/s	Yaw Angle, deg	Pitch Angle	RPM
3DR SOLO	0.48	20	N/A	-40 – 40	4,600 – 6,800
	1.9	40	N/A	-40 – 0	5,700 – 6,800
	7.7	80	N/A	-40 – -20	5,700 – 8,600
	0 (hover)	0	N/A	0	2,500 – 8,000
DJI Phantom 3	0 (hover)	0	N/A	0	2,500 – 8,000
3DR Iris+	0 (hover)	0	N/A	0	2,500 – 8,000
Drone America x8	0.48	20	N/A	-10 – 0	6,200 – 8,400
	1.9	40	N/A	-20 – 0	6,200 – 8,400
	0 (hover)	0	N/A	0	2,500 – 8,500
SUI Endurance	0.48	20	N/A	-20 – 0	2,800 – 4,200
	0 (hover)	0	N/A	0	2,000 – 4,500